A comprehensive climate history of the last 800 thousand years

Mario Krapp*[1], Robert Beyer[1], Stephen L. Edmundson[1,2], Paul J. Valdes[3], and Andrea Manica[1]

[1]University of Cambridge
[2]Utrecht University
[3]University of Bristol
*contact: *mariokrapp@gmail.com*

Abstract

A detailed and accurate reconstruction of past climate is essential in understanding the drivers that have shaped species, including our own, and their habitats. However, spatially-detailed climate reconstructions that continuously cover the Quaternary do not yet exist, mainly because no paleoclimate model can reconstruct regional-scale dynamics over geological time scales. Here we develop a new approach, the Global Climate Model Emulator (GCMET), which reconstructs the climate of the last 800 thousand years with unprecedented spatial detail. GCMET captures the temporal dynamics of glacial-interglacial climates as an Earth System Model of Intermediate Complexity would whilst resolving the local dynamics with the accuracy of a Global Climate Model. It provides a new, unique resource to explore the climate of the Quaternary, which we use to investigate the long-term stability of major habitat types. We identify a number of stable pockets of habitat that have remained unchanged over the last 800 thousand years, acting as potential long-term evolutionary refugia. Thus, the highly detailed, comprehensive overview of climatic changes through time delivered by GCMET provides the needed resolution to quantify the role of long term habitat fragmentation in an ecological and anthropological context.

Current patterns of diversification within and between species, such as our own [1], and the structuring of whole ecosystems can only be studied in the context of past climatic changes that have shaped them through time [2]. A detailed understanding of such processes has become an urgent necessity in order to predict responses to global change. However, whilst predictions of climate change and their impacts over the next few tens or hundreds of years are based on comprehensive Global Climate Models (GCMs) that resolve processes at high temporal and spatial resolution, such as those used in the latest IPCC Assessment Report [3], reconstructions back in time are challenging as they have to span a much longer period. GCMs can provide snapshots for a specific time or short transients in the order of a few thousands of years, whilst periods of tens or hundreds of thousands of years can only be covered with Earth System Models of Intermediate Complexity (EMICs) [4, 5], at the cost of low spatial resolution and a simplified representation of the climate system [6]. Neither of those two types of models is intentionally designed for paleo-ecology or species evolution, disciplines that require appropriate temporal scales of up to hundreds of thousands of years and spatial scales down to tens of kilometres.

Here, we fill this gap for a long-term reconstruction of climate that resolves regional-scale dynamics by reconstructing the last 800 thousand years (ka) at an unprecedented spatial resolution of approximately

1°. Unlike previous emulator approaches [7, 8], we explicitly focus on the local emulation of climate, which allows us to critically evaluate the reconstructed 800 ka of climate history against proxy records. Our approach consists of two steps (Fig. 1): a first reconstruction of the global climate at moderate spatial resolution followed by a more detailed representation of local dynamics using multiple snapshot simulations from the family of HadCM3 climate models [9]. In the first step, we use 72 simulations covering the past 120 ka from the HadCM3 climate model [10, 11], and build a linear regression model that acts as a GCM emulator (GCMET). GCMET accurately predicts the output of HadCM3 given a set of boundary conditions that is representative of as observed in the Middle and Late Pleistocene (details about this approach are found in the *Methods*). The logic behind our approach is that variations of a climate variable X (e.g. temperature) at any given location can be explained by variations in the external forcings. For the HadCM3 snapshots, the most important forcings are atmospheric CO_2 and the orbital parameters, i.e., precession, obliquity, and eccentricity. Other boundary conditions are Northern Hemisphere ice sheets and respective global sea-level changes (see [10] for details). The spatial model resolution after this first step is the same as of HadCM3, i.e., about 3° (3.75°×2.5°), henceforth referred to as GCMET-LO.

Results and discussion

We tested how well GCMET-LO matches HadCM3 snapshots by splitting them into a training and a test set (see *Methods* for details). Predicted mean annual temperatures (MAT) for the test set were within ca. 2 K (estimated as root mean square error, RMSE) to the output of HadCM3 for most parts of the globe (Fig. 2a) (a more thorough discussion is provided in the *Methods*). Mean annual precipitation (MAP) turned out to be less predictable but this was expected: temperature is a direct response to forcing whereas the precipitation response depends on multiple variables. We improved the MAP predictions substantially by using temperature and specific humidity as independent variables instead of CO_2 and orbital parameters (Extended Data Figure 1), and thereby reduced the average RMSE to from 9.3% down to 5.9%. Importantly, the discordance between HadCM3 and GCMET-LO are much smaller than the ensemble variability among different models in the Coupled Model Inter-comparison Project, Phase 5, and thus within the ranges of acceptable model uncertainties [3].

In the second step, we increase the resolution of our reconstructions to about 1° (1.25°×0.83°) using high resolution HadAM3H (Hadley Centre Atmospheric Model 3, High resolution) simulations covering the period of the last deglaciation. We computed high-resolution difference maps between equivalent HadAM3H and GCMET-LO snapshots (see *Methods* for details) and then created interpolated maps for any level of CO_2 (given the limited number of observations, we focus on CO_2 as the main driver of those differences). Those maps were added to GCMET-LO to obtain high resolution reconstructions, which we henceforth refer to simply as GCMET. To illustrate the importance of higher spatial variability, we compared GCMET, GCMET-LO, and LOVECLIM (an EMIC with a horizontal resolution of ca 5.5°×5.5°) to present-day observations (ERA-20C re-analysis 1961–1990 average [12]). LOVECLIM and GCMET-LO fail to capture the observed continental climate patterns whereas GCMET resolves those spatial features well (Fig. 3b).

Proxy comparison

We tested the ability of GCMET to capture changes in climate over the last 800 ka by comparing its predictions to a number of proxies (for a detailed comparison with proxy records, we refer to the *Methods*), using LOVECLIM [5] as a benchmark. As forcings we used CO_2 estimates from EPICA Dome C (EDC3) ice core [13], numerical solutions for the orbital parameters [14], whilst global sea-level changes and the distribution of the major Northern Hemisphere ice sheets were taken from a transient CLIMBER-2 climate simulation [4] and from the ICE-6G data set [15] (see *Methods* for details). We compared MAT to terrestrial proxies and to sea surface temperatures (SST) estimates based on marine proxies: GCMET is in agreement with a number of marine records (Fig. 3a–c, time series of all used proxies are shown in Extended Data Figures 2 & 3), with a mean RMSE of 1.5 K for all SST proxies and a mean correlation of 0.54, significantly larger (paired t-test: t_{38}=2.9, p=0.006) than for LOVECLIM (r=0.49, Fig. 3b). Despite the diverse nature of the terrestrial proxies (e.g. speleothems, loess, pollen), GCMET performance was as good as for marine proxies (r=0.52, Fig. 3b & d).

GCMET can also be used to reconstruct the climate in the deeper past, for example, by going back 2 million years (Ma). For this deeper past only a point-wise CO_2 reconstruction is available [16] which can be used to complement the quasi-continuous EDC3 CO_2 record covering the last 800 ka. The GCMET reconstructed global average MAT over the last 2 Ma shows a remarkable agreement with a global mean temperature proxy record [17] (correlation r=0.85 & RMSE=1.0 K, Fig. 3a). The predictive power over the last 2 Ma may seems surprising given that we do not have any HadCM3 snapshots before 120 ka ago. However, it is important to note that the phase space of the external forcings, CO_2 and orbital variations, is well covered, especially over the last 800 ka, by the last glacial cycle (see Extended Data Figure 4) and thus, we are mostly interpolating in a statistical sense.

Past habitat stability

The spatially detailed reconstructions provided by GCMET allow us to explore the effect of climate on habitats and species over time. We investigated ecosystem stability (Fig. 4) over the last 800 ka, focussing on the 14 major terrestrial habitats as defined by the WWF *Global 200* [18] (Fig. 4a). The reconstructions which are based on a random forest classifier [19] (see *Methods* for more details) show marked patterns in stability depending on location, with sparsely vegetated regions such as deserts among the most stable habitats in the world, the others being the core tropical rainforests along the equator. Large parts of Eurasia and North America are rendered unstable by the advancing and retreating Northern Hemisphere ice sheets with ecosystems alternating between vast forests during the warm interglacials and large tundras during the cold glacials (an animated version of the habitat changes throughout the last 800 ka is available as *Supplementary Video*). However, a few fragmented core boreal forest habitats remain. At the other end of the spectrum, unstable habitats as found in Subsaharan Africa support the idea that large scale habitat fragmentation have played a key role in the evolution of our species, *homo sapiens* [1].

A major advantage of GCMET is that it is computationally inexpensive. Thus, GCMET can not only produce high quality reconstructions of the last 800 ka, but also quantify and explore uncertainties in the external forcings, e.g., atmospheric CO_2, as we did by going back to 2 Ma. In doing so, we reconstructed the equivalent of hundreds GCM snapshots, a prohibitive endeavour for the foreseeable future. A way to understand the excellent fit of GCMET predictions against time series of climate proxies is that our approach captures the slow manifold of the stochastic climate system, thus allowing us to efficiently describe the behaviour over the longer, millennial, time scales. In turns, this implies that the glacial-interglacial climate of the Middle and Late Pleistocene responded in a consistent manner to orbital forcings and CO_2. It will interesting in the future to test whether this approximation holds for the Early Pleistocene with its faster ice age cyclicity of 41 ka; for this endeavour, we currently lack enough of estimates for CO_2 before the Mid-Pleistocene Transition, but GCMET is fully capable of covering the appropriate time periods if enough estimates become available. For the moment, we can offer a detailed, coherent reconstruction of the past 800 thousand years, which allowed us to pinpoint long-term potential refugia that have been characterised by the same habitat, and we expect that this will open up new ways to study the impact of past climate in a number of disciplines such as ecology and anthropology.

Methods

The global climate model emulator GCMET

The multiple linear regression model of GCMET-LO GCMET is derived from 72 available HadCM3 snapshot simulations [10, 11] (`https://www.paleo.bristol.ac.uk/ummodel/data/tdwza/standard_html/tdwza.html`, last accessed on 05 Oct 2018). It is a linear regression model for each individual model grid box with the following independent variables: atmospheric CO_2 concentrations as a major greenhouse gas, and eccentricity, obliquity, and precession as orbital parameters [14]. The sine function has been applied to the precession parameter which is expressed as longitude of the perihelion (in degrees) to make it a continuous function (was in degrees). Atmospheric CO_2 concentrations are the same as in the respective HadCM3 time slice simulation, e.g., 280 ppmv for 0 ka before present (BP). The available 72 HadCM3 simulations cover the last 120,000 years in 2,000-year intervals from 120,000 to 24,000 ka BP and in 1,000-year intervals from 22,000 to present-day.

The dependent variables are temperature T, precipitation P, or specific humidity Q. All independent variables, i.e., the predictors, are applied as normalised forcings. Thus, the resulting regression coefficients, or β coefficients, can be compared across different climate variables, i.e., temperature and precipitation, and across each other (Extended Data Figures 5–7).

Variations of a climate variable X based on a multiple linear regression model for the deviations from the mean, i.e., the anomalies X', such that $X = \overline{X} + X'$ with $\overline{X}$ being the mean of X. The equation for X' then is:

$$X'(x,y,t) = \beta_{CO_2}(x,y)CO_2'(t) + \beta_\varepsilon(x,y)\varepsilon'(t) + \beta_e(x,y)e'(t) + \beta_\Omega(x,y)\Omega'(t) \tag{1}$$

In this equation the βs are the regression coefficients for the respective predictor. CO_2 describes atmospheric CO_2 concentrations. ε denotes obliquity, e eccentricity, and Ω the sine of the longitude of the perihelion, i.e., the precessional component of Earth's orbit around the sun. The prime ($'$) denotes the anomalies from the mean. The variables x, y, and t represent the spatial, i.e., longitude and latitude, and the time coordinates. To make the linear regression well-conditioned, all independent variables have been normalised, i.e., the mean has been subtracted and the data has then been divided by their standard deviation. To prevent our linear regression model from predicting negative precipitation values, we apply a logarithmic transformation first. For bounded variables such as precipitation this is a common procedure. In the case of precipitation, the linear regression coefficients are predicting the response in terms of anomalies in the exponent. For similar reasons we transform specific humidity using the logit functions, $\mathrm{logit}(x) = \log(\frac{x}{1-x})$, which maps values from [0,1] to $[-\infty, +\infty]$; the units of specific humidity are [kg/kg] and its values fall in the range between 0 and 1. The decomposition of temperature T, precipitation P, and specific humidity Q into anomalies, i.e., the X' on the left hand side of Eq. 1 is:

$$T = \overline{T} + \underbrace{T'}_{\hat{=}X'} \tag{2}$$

$$\log P = \overline{\log P} + \underbrace{(\log P)'}_{\hat{=}X'} \tag{3}$$

$$\operatorname{logit} Q = \overline{\operatorname{logit} Q} + \underbrace{(\operatorname{logit} Q)'}_{\hat{=}X'} \tag{4}$$

We also consider changes in surface type, i.e., ocean, land, and ice. For example, around the coastlines, land can turn into ocean due to rising sea levels and vice versa, or the expanding ice sheets turn land into ice. Both, precipitation and temperature respond to different surface type in a different way. Therefore, each of the surface types (ocean, land, and ice) yields a distinct linear regression model.

For the improved precipitation model (as mentioned in the main text) we used temperature T and specific humidity Q as independent variables

$$X' = (\log P)' = \beta_T T' + \beta_Q (\operatorname{logit} Q)' \tag{5}$$

This leads to precipitation predictions with a lower root mean square error over land (it is also explained below and shown in Extended Data Figure 1). For the predicition of the climate before 120 ka BP this means that we first need to reconstruct T and Q, and then we can use the β coefficients for T and Q to reconstruct P.

In contrast to existing emulator approaches [7, 8, **?**], we provide local-scale reconstructions which lead to reasonable aggreement with existing palaeo-climate proxies as shown by the comprehensive model–data comparison. Furthermore, because the parameter sampling is based on realistic glacial cycle snapshot simulations, the obtained regression coefficients are good enough approximation to predict previous glacial–interglacial climate states well.

Training and test data To make useful predictions and to evaluate the skill of our model, we need to have an independent test data set. A sensible choice is to use 80% of the data for the training of a model and 20% for the aforementioned test of the model. For a 80%/20% division of the 72 time slices into training and test data, i.e., 14 or 58 out of 72, there are $\binom{n}{k} = \binom{72}{58} \approx 3 \times 10^{14}$ possible combinations.

Instead of randomly dividing the data into the training/test data, we follow an approach with the aim to preserve as much variance as possible in the training data. The idea is to choose the parameter sets (i.e., the independent variables, not the dependent climate variables) in such a way that they retain the most variance. First, we derive the covariance matrix of the full parameter set (n=72) and calculate the eigenvalues of the covariance matrix. In the next step, we randomly create a training data set (k=58) for which we compute the covariance. If the covariance of this sample training set is larger than the full covariance matrix, i.e., the eigenvalues of the covariance matrix are larger than the eigenvalues of the covariance matrix of the full parameter set, this sample parameter set is marked as a candidate for the final training set. After several iterations (N=10,000), we sum up how many times each time slice has appeared within a candidate training set. We then rank all time slices according to this number. In the final step, we pick the 80% top-ranked time slices as training data.

Model validation For the model validation, we use R^2 values, a goodness of fit estimator of the training data, and the root mean squared error (RMSE), an estimator of the goodness of the model for the prediction of the test data (see Extended Data Figure 8). Overall, our linear model is a better predictor for temperature than for precipitation.

Temperature responds more directly to local forcings because temperature is determined by the energy balance of downward and upward longwave and shortwave radiation and turbulent heat fluxes. The downward shortwave radiation depends on the incoming solar radiation, which is determined by orbital variations, whereas the downward longwave radiation is determined by greenhouse gases such as CO_2 and water vapour, as well as by cloud cover. Large-scale circulation changes have a much smaller effect on temperature. It is therefore locally far better constrained by global CO_2 and orbital variations. This increases the predictive skill of our linear regression model substantially leading to high R^2 values and low RMSEs.

The matter is more complicated for precipitation because it is a consequence of the hydrological cycle, which itself depends mainly on large-scale atmospheric dynamics, such as the monsoonal systems in the tropics and subtropics, or the midlatitude storm systems. To a lesser extend do local interactions between the atmosphere and the surface, i.e., ocean, land, or ice play a role. Examples are evaporation and transpiration over the ocean, or deep convection over the tropics. Processes and circulation features like moisture transport or the atmospheric Hadley cell dynamics determine to a much larger extent the non-local response of precipitation to CO_2 or orbital variations. Because of the larger dynamical component of the hydrological cycle, as compared to temperature, precipitation is much less constrained by external forcings than temperature. Therefore, the linear regression model has less predictive skill for precipitation than for temperature. However, it turns out that the predictive skill for precipitation can be improved by using temperature and specific humidity as predictors instead of the orbital parameters and CO_2. By doing so the RMSEs can be substantially reduces, especially over land (Extended Data Figure 1).

The regression coefficients To get an idea of how reliable our estimate for predictors are, we calculate the p-values for each of the predictors, i.e., the beta coefficients. Here, the p-value tests the null hypothesis whether the coefficient is equal to zero, which means that the specific predictor has no effect. If the p-value is below a certain threshold—in our case below the 5% significance level: $p < 0.05$—the null hypothesis can be rejected. That means that the specific predictor is a meaningful addition to our linear regression model and any changes in the associated predictor are related to changes in the corresponding climate variable. Regions for which the null hypothesis cannot be rejected are displayed as shaded and hatched in Extended Data Figures 5–7. In these regions, we set the β coefficients to zero and the associated forcing has no effect.

Increasing to high resolution in GCMET Using nine high-resolution HadAM3H simulations, which cover the deglaciation since 21 ka BP (21, 18, 15, 12, 10, 8, 6, 3, and 0 ka BP), we are able to increase the spatial resolution from 3°, which is the spatial resolution of GCMET after the linear regression step (and the same as the coarse resolution of the original HadCM3 snapshots), to ca. 1°. We do so by calculating the difference between equivalent coarse- and high-resolution snapshots. For example, the difference at 10 ka BP is $\Delta_{10\,\mathrm{ka\,BP}} = HadAM3H_{10\,\mathrm{ka\,BP}} - HadCM3_{10\,\mathrm{ka\,BP}}$. We choose to interpolate the differences linearly according to their CO_2 levels, e.g., 231 ppm at 10 ka BP, because any statistical model with more than one variable would require more snapshots to adequately predict the differences. Thus, we simply assume that the differences between a coarse- and high-resolution climate can be explained as a function of the CO_2 forcing, i.e., $\Delta_{10\,\mathrm{ka\,BP}} = \Delta_{231\,\mathrm{ppm}}$. Now, for any period in the past, e.g., 300 ka BP, we add the high-resolution difference, i.e., the Δ, which corresponds to the respective CO_2 level, to the coarse-resolution reconstruction. Note that the downscaling approach captures the regional-scale dynamics of the GCM in this step, which change over time. This is in contrast to commonly used ”delta approach” for downscaling.

Boundary conditions: CO_2, global sea-level, and Northern Hemisphere ice sheets For realistic high-resolution reconstructions the model boundary conditions need to be known: atmospheric CO_2 levels, global sea levels (for the land-sea mask), and the extent of Northern Hemisphere (NH) ice sheets. The longest, quasi-continuous record of past CO_2 levels is the 800,000 years long CO_2 record from the EPICA Dome C ice core in Antarctica [13]. Before that we use point-wise CO_2 estimates that go back about 2 Ma [16], coinciding with the earliest time for which we are able to generate reasonable climate reconstructions (Extended Data Figure 9).

Because there are no self-consistent continuos reconstructions of NH ice sheets available that span the last 2 Ma, we use modelled NH ice sheet extents and heights which are available every 1 ka for the years from 800–123 ka BP from CLIMBER-2/SICOPOLIS simulations [4]. For the period from 122–0 ka BP we use the ice sheet configurations from the ICE-6G data set [15] (`http://www.atmosp.physics.utoronto.ca/~peltier/data.php`, last accessed 09.11.2018). For simplicity, we assume present-day ice sheets for any period before 800 ka BP. Topographic changes due to growing or shrinking ice sheets are derived from a global sea-level record [20] which have been added on top of present-day coast lines while preserving inland lakes.

Comparison with proxy reconstructions

Despite the increasing number of available paleoclimate proxies, only a small percentage can be used for a quantitative comparison to climate models because translating sediment core data into actual climate variables remains a difficult task. Marine sediment cores are the exception, as they are useful archives of sea surface temperature (SST). Because the associated biogeochemistry is relatively straightforward, marine proxies can be utilized as so-called paleo-thermometers and are thus well suited for a direct proxy–model comparison. For these proxies, we make a direct comparison between MAT and SST, quantified both in terms of correlation between the predicted and observed time series and the RMSE. Note that MAT and SST are not the same climatological quantities; SST is the temperature of the ocean surface and has a lower limit of about -1.8°C, the freezing point of saltwater. While we expect MAT and SST to co-vary in low and mid-latitudes, at higher latitudes seasonal or permanent sea ice could make a straitforward comparison between both variables problematic.

For terrestrial proxies, for which a translation into climatic variables is not straightforward, we simply quantify the correlation between the two standardized time series without a more detailed error quantification in terms of the RMSE. However, the interpretation of terrestrial of climate proxies can also be problematic. For example, pollen-based vegetation reconstructions are suggested to be less reliable as climate proxies, particularly for interglacials [21].

We have assembled existing long-term SST proxy reconstructions (see Extended Data Figure 2) which cover at least a period of about 150 ka BP during the Middle and Late Pleistocene (specifically, the last 800ka, for which we can reconstruct the climate continuously).

Ecosystem reconstructions

We use a random forest classifier [19, 22] which is trained by a set of four climate variables from GCMET: minimum and mean annual temperature, and minimum and mean annual precipitation, to reconstruct the present-day distribution of the 14 ecoregions. The required present-day data has been split into a training (80%) and a test data set (20%). The classification factors from this training data set were then applied to predict ecosystem changes of the last 800,000 years.

The goodness of the predictions by the random forest classifier can be estimated by the so-called receiver operating characteristic (ROC, see Extended Data Figure 10). A ROC curve displays the true positive rate against the false positive rate and the closer that curve is to the upper left corner, the better the prediction for a specific ecosystem is. For example, the point at coordinate (0,1) represents the best possible prediction with 100% sensitivity (i.e., no false negatives) and 100% specificity (i.e., no false positives). The diagonal line depicts a prediction by random guessing.

The random forest classification is very close to perfect classification for the average of all ecosystem types and the area under the curve (also given in the legend to Extended Data Figure 10) is an estimator for the goodness of the classification. Except for a few instances, such as for ”Tropical & Subtropical Coniferous Forests” and ”Mangroves”, this value is arger than 0.9 (average 0.98).

Data and model code availability

High-resolution climate data for the last 800 ka and 2 Ma A continuous climate data set for the last 800,000 years are publicly available at [link to data repository]. We included the following variables in 1,000 year intervals and in at a 1° horizontal resolution:

- mean annual temperature
- minimum annual temperature
- mean annual precipitation
- minimum annual precipitation
- mean annual specific humidity (needed for mean annual precipitation)
- minimum annual specific humidity (needed for minimum annual precipitation)
- 14 major habitats according to the *global 200* defined by the WWF
- 3 aggregated ecosystem classifications (from the 14 major habitats): ”open habitat”, ”forests”, and ”sparsely vegetated”

For the reconstruction if the 2 Ma with the sporadic CO_2 records (52 time steps) we provide the following variables:

- mean annual temperature (ensemble mean, n=50)
- mean annual temperature (ensemble standard deviation, n=50)

GCMET and proxy time series The data generated for the individual time series comparisons of GCMET and proxy records (Extended Data Figures 2 & 3) is also publicly available as an MS Excel file at [link to data repository].

GCMET model code, analysis, and visualisation scripts The model code for GCMET as well as the code for the analysis and visualisation of figures [23, 24] is publicly available at [link to model repository].

Author contributions

AM and MK devised the project; MK devised and implemented the emulator with input from RB and SLE. PJV provided additional HadCM3 snapshot simulations. MK and AM wrote a first draft of the paper which was improved by input from all other authors; MK wrote the methods and prepared the figures.

Competing interests

The authors declare no competing interests.

Acknowledgements

This work was supported by an ERC Consolidator Grant to AM (Local Adaptation 647787).

References

[1] Eleanor M. L. Scerri, Mark G. Thomas, Andrea Manica, Philipp Gunz, Jay T. Stock, Chris Stringer, Matt Grove, Huw S. Groucutt, Axel Timmermann, G. Philip Rightmire, Francesco d'Errico, Christian A. Tryon, Nick A. Drake, Alison S. Brooks, Robin W. Dennell, Richard Durbin, Brenna M. Henn, Julia Lee-Thorp, Peter deMenocal, Michael D. Petraglia, Jessica C. Thompson, Aylwyn Scally, and Lounès Chikhi. Did Our Species Evolve in Subdivided Populations across Africa, and Why Does It Matter? *Trends in Ecology & Evolution*, 33(8):582–594, August 2018.

[2] Michael Doebeli and Ulf Dieckmann. Speciation along environmental gradients. *Nature*, 421(6920):259–264, January 2003.

[3] S. Solomon, D. Qin, M. Manning, Z. Chen, M. Marquis, K. Avery, M. Tignor, and H. Miller, editors. *IPCC: Climate Change 2007: The Physical Science Basis. Contribution of Working Group I to the Fourth Assessment Report of the Intergovernmental Panel on Climate Change*. Cambridge University Press, 2007.

[4] A. Ganopolski and R. Calov. The role of orbital forcing, carbon dioxide and regolith in 100 kyr glacial cycles. *Clim. Past*, 7(4):1415–1425, December 2011.

[5] Axel Timmermann, Tobias Friedrich, Oliver Elison Timm, Megumi O. Chikamoto, Ayako Abe-Ouchi, and Andrey Ganopolski. Modeling Obliquity and CO2 Effects on Southern Hemisphere Climate during the Past 408 ka. *J. Climate*, 27(5):1863–1875, November 2013.

[6] M. Claussen, L. Mysak, A. Weaver, M. Crucifix, T. Fichefet, M.-F. Loutre, S. Weber, J. Alcamo, V. Alexeev, A. Berger, R. Calov, A. Ganopolski, H. Goosse, G. Lohmann, F. Lunkeit, I. Mokhov, V. Petoukhov, P. Stone, and Z. Wang. Earth system models of intermediate complexity: closing the gap in the spectrum of climate system models. *Climate Dynamics*, 18(7):579–586, March 2002.

[7] P. A. Araya-Melo, M. Crucifix, and N. Bounceur. Global sensitivity analysis of the Indian monsoon during the Pleistocene. *Clim. Past*, 11(1):45–61, January 2015.

[8] Natalie S. Lord, Michel Crucifix, Dan J. Lunt, Mike C. Thorne, Nabila Bounceur, Harry Dowsett, Charlotte L. O'Brien, and Andy Ridgwell. Emulation of long-term changes in global climate: application to the late Pliocene and future. *Climate of the Past*, 13(11):1539–1571, November 2017.

[9] P. J. Valdes, E. Armstrong, M. P. S. Badger, C. D. Bradshaw, F. Bragg, M. Crucifix, T. Davies-Barnard, J. J. Day, A. Farnsworth, C. Gordon, P. O. Hopcroft, A. T. Kennedy, N. S. Lord, D. J. Lunt, A. Marzocchi, L. M. Parry, V. Pope, W. H. G. Roberts, E. J. Stone, G. J. L. Tourte, and J. H. T. Williams. The BRIDGE HadCM3 family of climate models: HadCM3@Bristol v1.0. *Geosci. Model Dev.*, 10(10):3715–3743, October 2017.

[10] Joy S. Singarayer and Paul J. Valdes. High-latitude climate sensitivity to ice-sheet forcing over the last 120kyr. *Quaternary Science Reviews*, 29(1):43–55, 2010. 00092.

[11] T. Davies-Barnard, A. Ridgwell, J. Singarayer, and P. Valdes. Quantifying the influence of the terrestrial biosphere on glacial–interglacial climate dynamics. *Clim. Past*, 13(10):1381–1401, October 2017.

[12] Paul Poli, Hans Hersbach, Dick P. Dee, Paul Berrisford, Adrian J. Simmons, Frédéric Vitart, Patrick Laloyaux, David G. H. Tan, Carole Peubey, Jean-Noël Thépaut, Yannick Trémolet, Elías V. Hólm, Massimo Bonavita, Lars Isaksen, and Michael Fisher. ERA-20c: An Atmospheric Reanalysis of the Twentieth Century. *J. Climate*, 29(11):4083–4097, March 2016.

[13] Bernhard Bereiter, Sarah Eggleston, Jochen Schmitt, Christoph Nehrbass-Ahles, Thomas F. Stocker, Hubertus Fischer, Sepp Kipfstuhl, and Jerome Chappellaz. Revision of the EPICA Dome C CO2 record from 800 to 600 kyr before present. *Geophys. Res. Lett.*, 42(2):2014GL061957, January 2015.

[14] A. Berger and M. F. Loutre. Insolation values for the climate of the last 10 million years. *Quaternary Science Reviews*, 10(4):297–317, January 1991.

[15] W. R. Peltier, D. F. Argus, and R. Drummond. Space geodesy constrains ice age terminal deglaciation: The global ICE-6g_c (VM5a) model. *Journal of Geophysical Research: Solid Earth*, 120(1):450–487, November 2014.

[16] Bärbel Hönisch, N. Gary Hemming, David Archer, Mark Siddall, and Jerry F. McManus. Atmospheric Carbon Dioxide Concentration Across the Mid-Pleistocene Transition. *Science*, 324(5934):1551–1554, June 2009.

[17] Carolyn W. Snyder. Evolution of global temperature over the past two million years. *Nature*, 538(7624):226–228, October 2016.

[18] David M. Olson, Eric Dinerstein, Eric D. Wikramanayake, Neil D. Burgess, George V. N. Powell, Emma C. Underwood, Jennifer A. D'amico, Illanga Itoua, Holly E. Strand, John C. Morrison, Colby J. Loucks, Thomas F. Allnutt, Taylor H. Ricketts, Yumiko Kura, John F. Lamoreux, Wesley W. Wettengel, Prashant Hedao, and Kenneth R. Kassem. Terrestrial Ecoregions of the World: A New Map of Life on EarthA new global map of terrestrial ecoregions provides an innovative tool for conserving biodiversity. *BioScience*, 51(11):933–938, November 2001.

[19] Leo Breiman. Random Forests. *Machine Learning*, 45(1):5–32, October 2001.

[20] R. M. Spratt and L. E. Lisiecki. A Late Pleistocene sea level stack. *Clim. Past*, 12(4):1079–1092, April 2016.

[21] Ulrike Herzschuh, H. John B. Birks, Thomas Laepple, Andrei Andreev, Martin Melles, and Julie Brigham-Grette. Glacial legacies on interglacial vegetation at the Pliocene-Pleistocene transition in NE Asia. *Nature Communications*, 7:11967, June 2016.

[22] F. Pedregosa, G. Varoquaux, A. Gramfort, V. Michel, B. Thirion, O. Grisel, M. Blondel, P. Prettenhofer, R. Weiss, V. Dubourg, J. Vanderplas, A. Passos, D. Cournapeau, M. Brucher, M. Perrot, and E. Duchesnay. Scikit-learn: Machine Learning in Python. *Journal of Machine Learning Research*, 12:2825–2830, 2011.

[23] J. D. Hunter. Matplotlib: A 2d graphics environment. *Computing In Science & Engineering*, 9(3):90–95, 2007.

[24] Met Office. Cartopy: a cartographic python library with a Matplotlib interface, 2010.

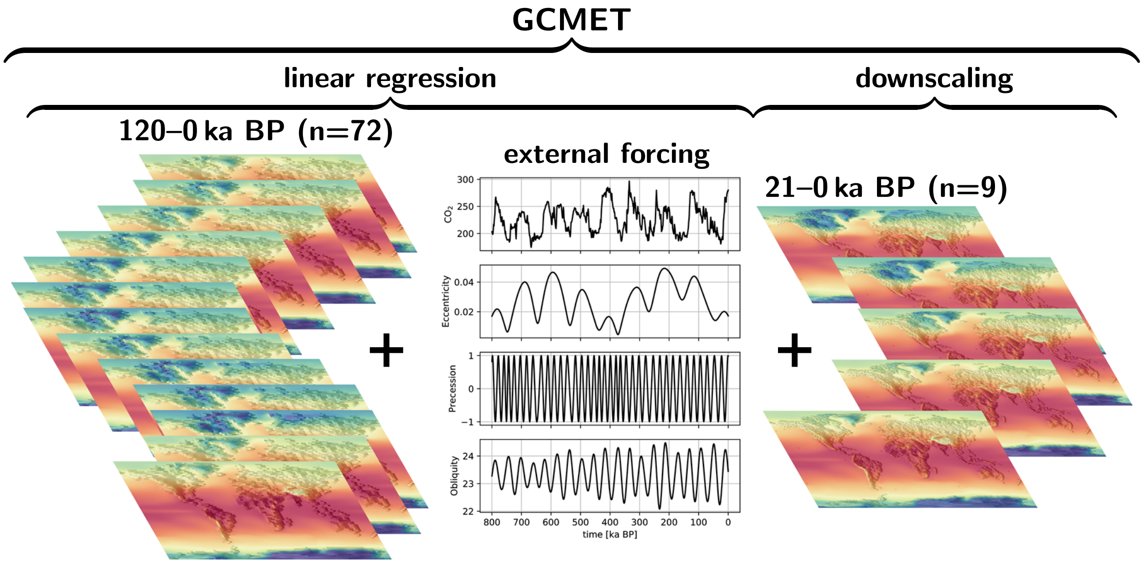

Figure 1: Schematic of the GCMET components: A linear regression combines 72 HadCM3 snapshot simulations with the external forcings, i.e., CO_2 and the three orbital parameters, which provides the basis of the long-term climate reconstructions of the last 800 thousand (or 2 million) years. Using 9 high-resolution snapshots covering the last deglaciation provides the basis of the downscaling approach based on CO_2 which yields the final high-resolution long-term climate reconstructions of GCMET.

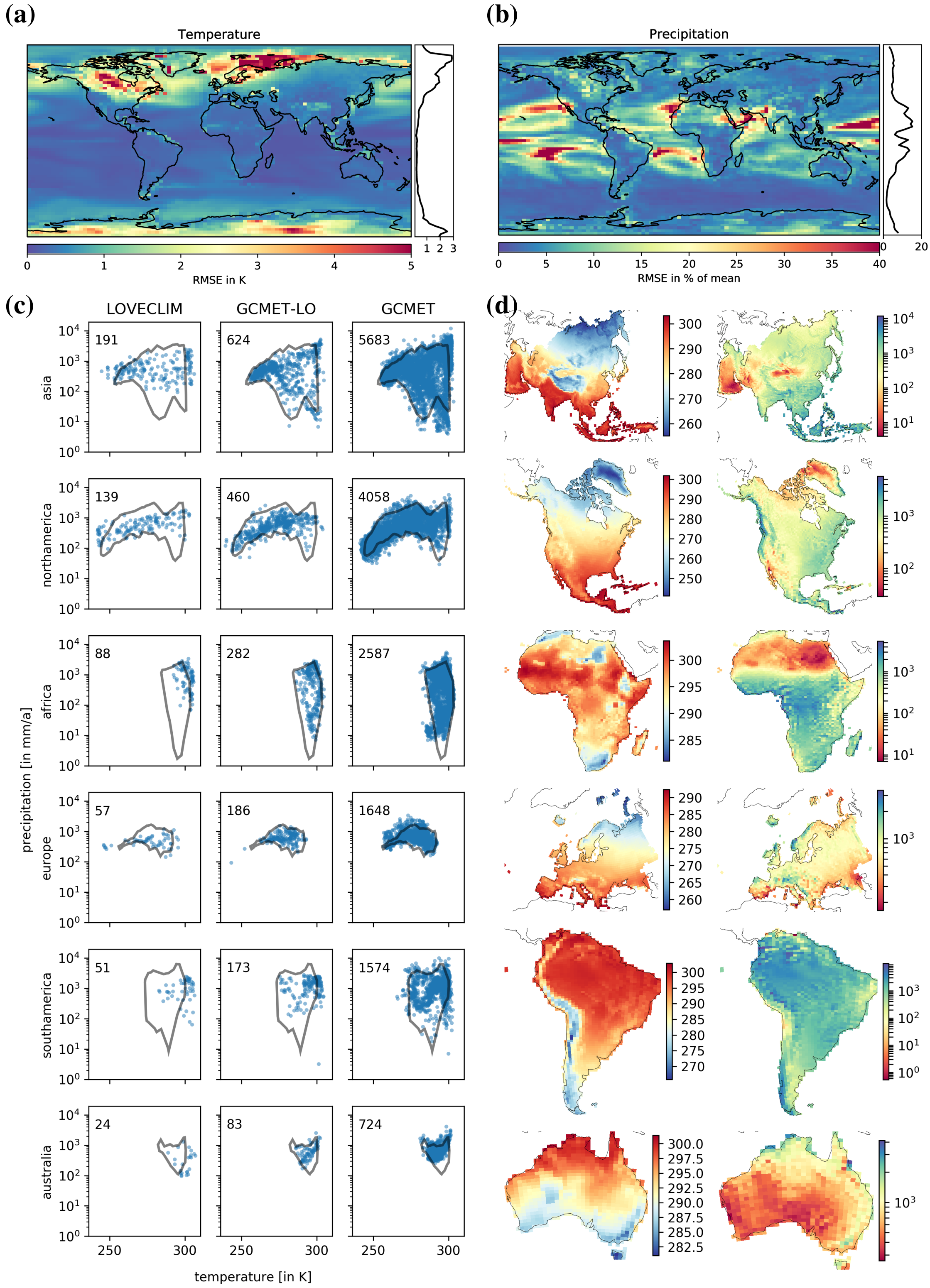

Figure 2: Root mean square error of the GCMET-LO predictions for the 14 HadCM3 snapshots for (a) MAT and (b) MAP (lower is better). (c) Present-day, i.e., 0 ka BP, temperature–precipitation phase diagram for Asia, North America, Africa, Europe, South America, and Australia, as modelled by LOVE-CLIM and reconstructed by GCMET-LO and GCMET and compared to observed multi-annual mean values (grey contours) for the period from 1961-1990 [12]. The numbers in each plot indicate the number of grid points covering the respective continent. (d) Maps of present-day temperature (in K) and precipitation (in mm/a) as reconstructed by GCMET for the six continents.

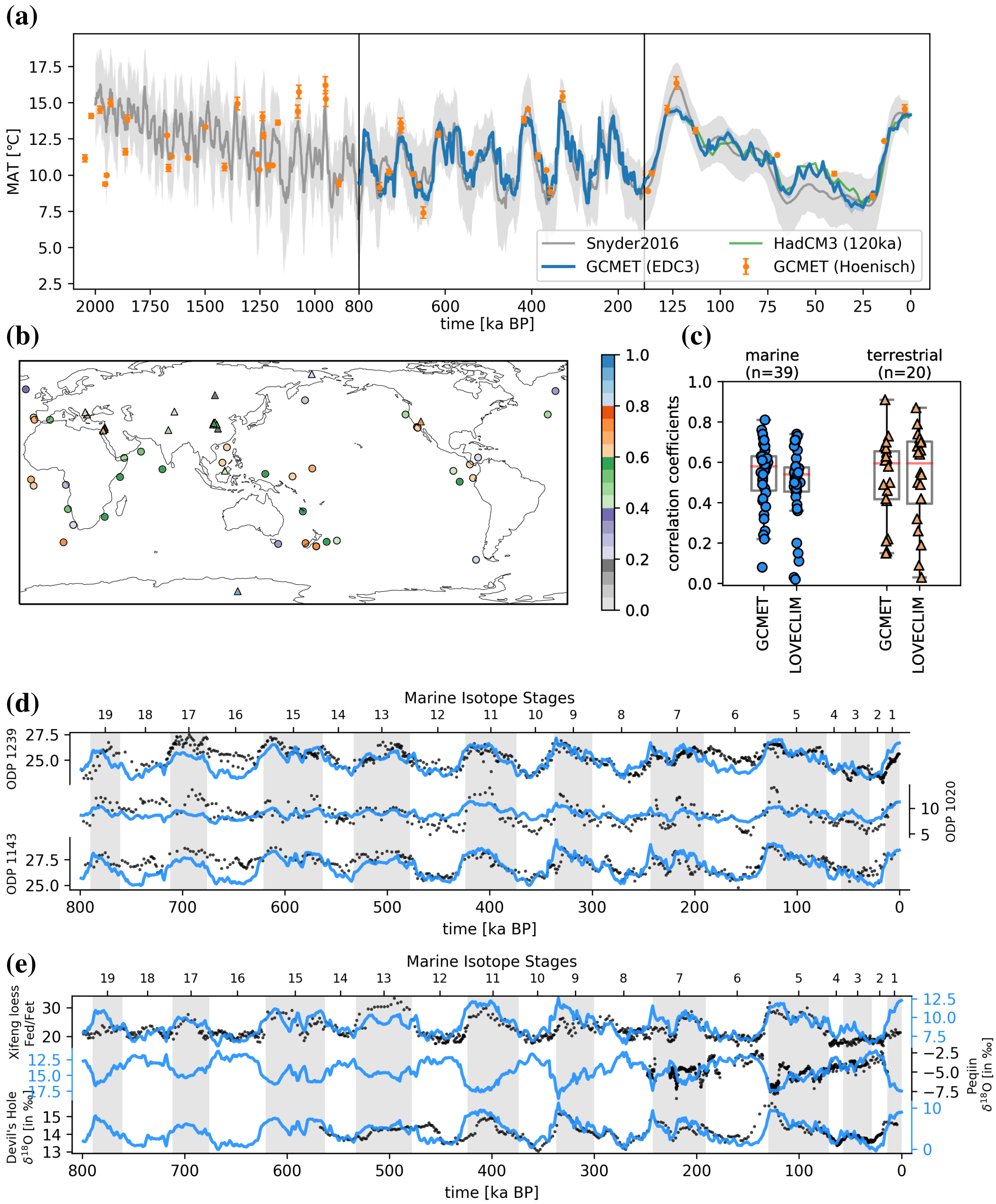

Figure 3: (a) Global mean temperature for the last 2 Ma as predicted by GCMET based on different CO_2 records in comparison with a proxy-based global mean temperature reconstruction [17]. Furthermore, the time series from the 72 HadCM3 snapshots for the last 120 ka have also been added. Note the change in the spacing of the time axis at 800 ka and 140 ka BP. (b) Map of correlation coefficients between marine (in terms of as sea surface temperature) and terrestrial climate proxy time series and mean annual temperatures as reconstructed by GCMET-LO for the respective locations. The individual time series and references for the proxies can be found in the Extended Data Table 1, Extended Data Figures 2 & 3 and in the *Methods*. (c) Box plots showing the range of correlations between GCMET (LOVECLIM) and the respective marine and terrestrial proxies. Time series of three selected (d) marine and (e) terrestrial proxies and the corresponding reconstructions by GCMET. While marine proxies are plotted on the same y axis, different scales have been used for terrestrial proxies.

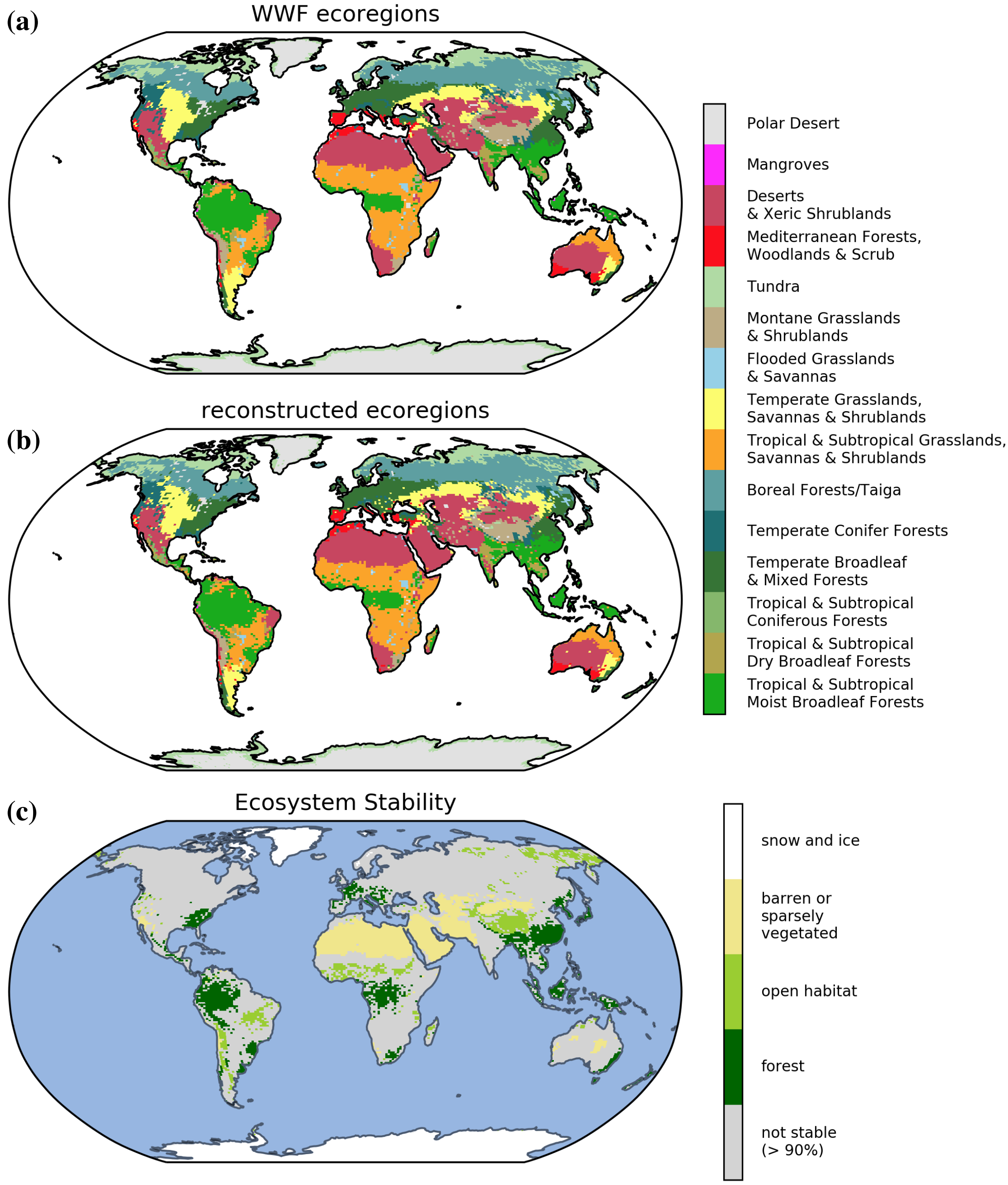

Figure 4: (a) Map of 14 major terrestrial habitats as defined by the WWF [18] for present-day and (b) as reconstructed with GCMET inputs of minimum and annual temperature and minimum and annual precipitation. (c) Stability of open habitats, such as grasslands and savannahs, and forest habitats, and sparsely vegetated regions across the world through the last 800,000 years. Regions in which the habitats have been unstable, i.e., of different type, for more than 90% are coloured in grey.

	core/name	location	lon	lat	type	reference
marine proxies	HY04	Eastern Equatorial Pacific	-95.0	4.0	SST	[25, 26]
	MD06-2986	Tasman Sea	167.9	-43.4	SST	[25, 27]
	ODP1125	Southwestern Pacific	-178.2	-42.6	SST	[28]
	ODP1123	Southwestern Pacific	-171.5	-41.8	SST	[25, 29]
	ODP846	Eastern Equatorial Pacific	-90.8	-3.1	SST	[25, 30]
	ODP1239	Eastern Equatorial Pacific	-82.1	-0.7	SST	[31]
	ODP982	North Atlantic	-15.9	57.5	SST	[25, 32]
	ODP1020	Northeastern Pacific	-126.4	41.0	SST	[25, 33]
	ODP1146	South China Sea	116.3	19.5	SST	[25, 34]
	ODP1143	Western Equatorial Pacific	113.3	9.4	SST	[25, 35]
	ODP1090	Southeastern Atlantic	8.9	-42.9	SST	[25, 36]
	ODP1012	Northeastern Pacific	-118.4	32.3	SST	[25, 37]
	ODP1082	Southeastern Atlantic	11.8	-21.1	SST	[38]
	MD06-3018	Tropical Western Pacific	166.2	-22.6	SST	[39]
	ODP722	Arabian Sea	59.8	16.6	SST	[25, 34]
	ODP882	Northwestern Pacific	167.6	50.4	SST	[40]
	MD97-2140	Western Pacific Warm Pool	141.5	2.0	SST	[25]
	MD96-2048	Mozambique Channel	36.0	-26.2	SST	[41]
	ODP1172	Tasman Sea	149.9	-44.0	SST	[42]
	DSDP594	Southwest Pacific	175.0	-45.5	SST	[25, 43]
	DSDP607	North Atlantic	-33.0	41.0	SST	[25, 44]
	PS75034-2	Southeastern Pacific	-80.1	-54.4	SST	[25, 45]
	ODP871	Western Equatorial Pacific	172.3	5.6	SST	[46]
	ODP806B	Western Equatorial Pacific	159.4	0.3	SST	[25, 47]
terrestrial proxies	Baoji	China	107.1	34.4	rainfall	[48]
	Soreq	Israel	36.0	31.4	δ^{18}O	[49]
	Lake El'gygytgyn	Russia	172.0	67.5	χ	[50]
	Chanwu	China	107.7	35.2	δ^{18}O	[51]
	Dead Sea	Israel	35.0	30.5	lake level	[52]
	Devil's Hole	Nevada, USA	-116.3	36.4	δ^{18}O	[53]
	Tzavoa	Israel	35.2	31.2	δ^{18}O	[54]
	Yimaguan Luochuan	China	108.5	35.8	χ_{fd}	[25, 55]
	Weinan	China	108.8	34.4	MAT	[56]
	Negev	Israel	34.8	30.6	δ^{18}O	[54]
	Peqiin	Israel	36.0	32.6	δ^{18}O	[49]
	Xifeng	China	107.6	35.7	Fed/Fet	[51]
	EPICA Dome C	Antarctica	123.4	-75.0	ΔT	[57]
	Kesang	western China	81.8	42.9	δ^{18}O	[58]
	Clearwater	Borneo	114.9	4.1	δ^{18}O	[59]
	Tenaghi Philippon	Greece	24.2	41.0	pollen	[25, 60]
	Sanbao-Dongge	China	110.4	31.7	δ^{18}O	[61]

Extended Data Table 1: Marine and terrestrial proxy records that have been used in this study, their location, coordinates and the respective reference.

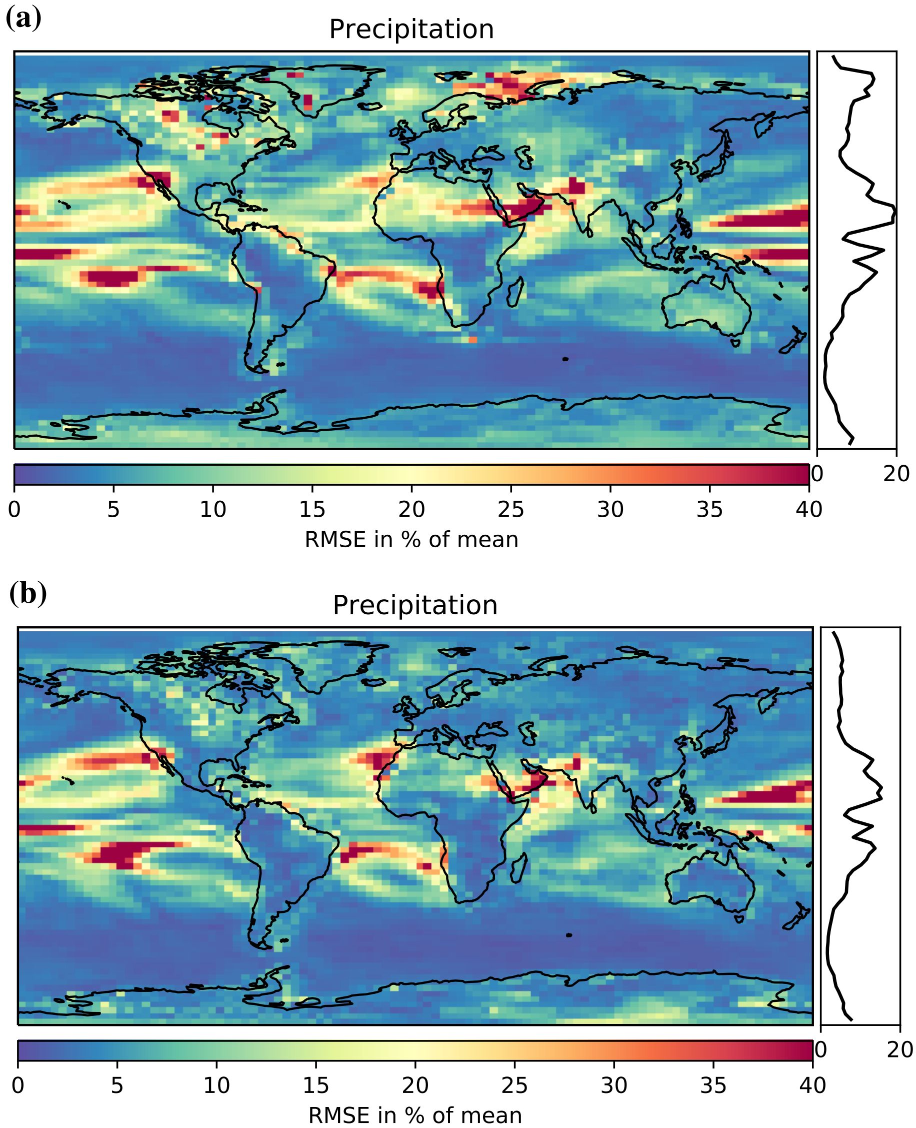

Extended Data Figure 1: Root mean square error of the GCMET-LO predictions for the 14 HadCM3 snapshots for mean annual precipitation with (a) CO_2 and orbital parameters as independent variables and (b) mean annual temperature and specific humidity as independent variables (lower values are better).

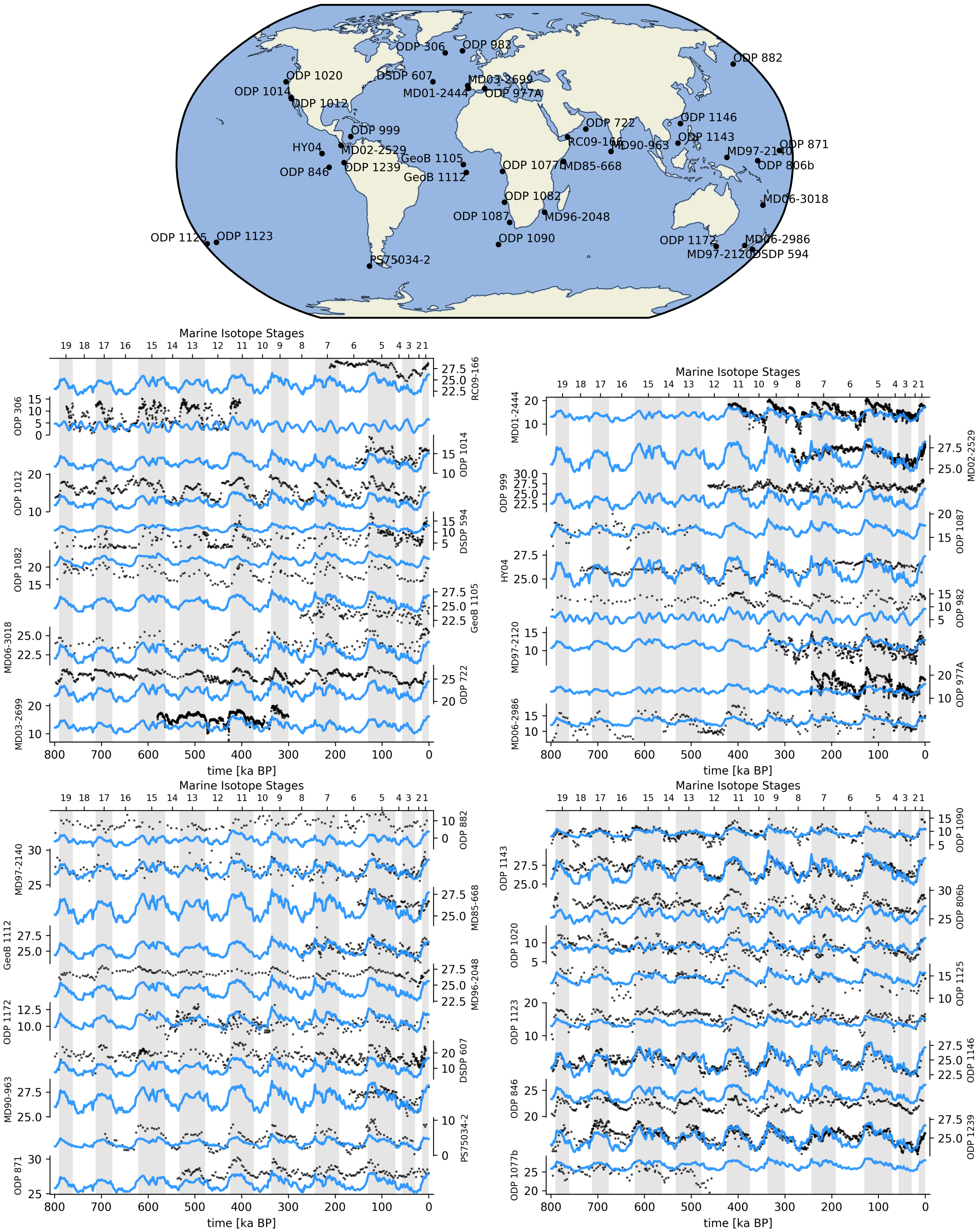

Extended Data Figure 2: Time series of 39 Middle and Late Pleistocene marine sea surface temperature proxies (black dots) and modelled mean annual temperature at their closest location (blue lines). Proxy–derived and model temperature are on the same scale, in °C).

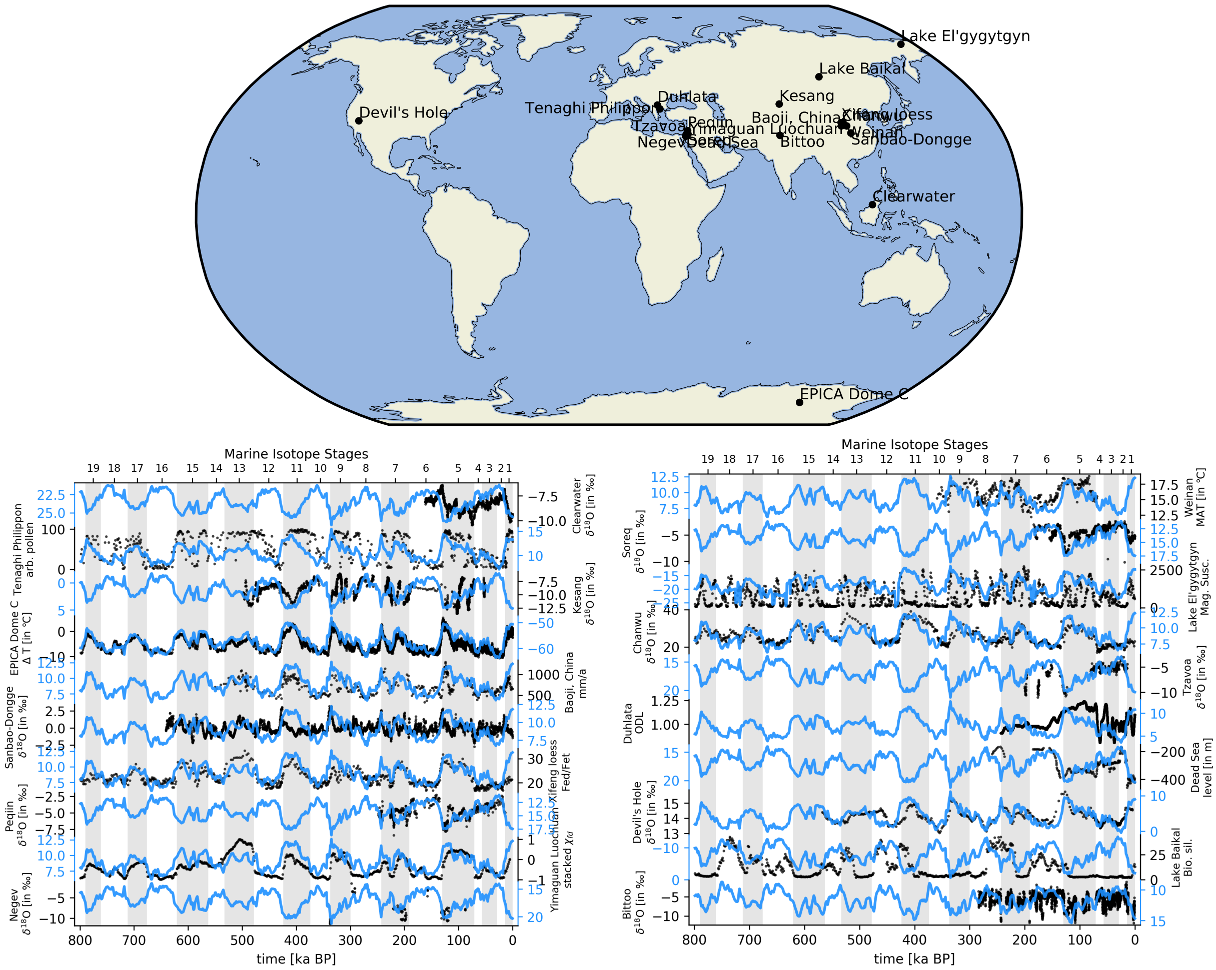

Extended Data Figure 3: Time series of 20 Middle and Late Pleistocene terrestrial proxies (black dots) and modelled mean annual temperature at their closest location (blue lines), in °C).

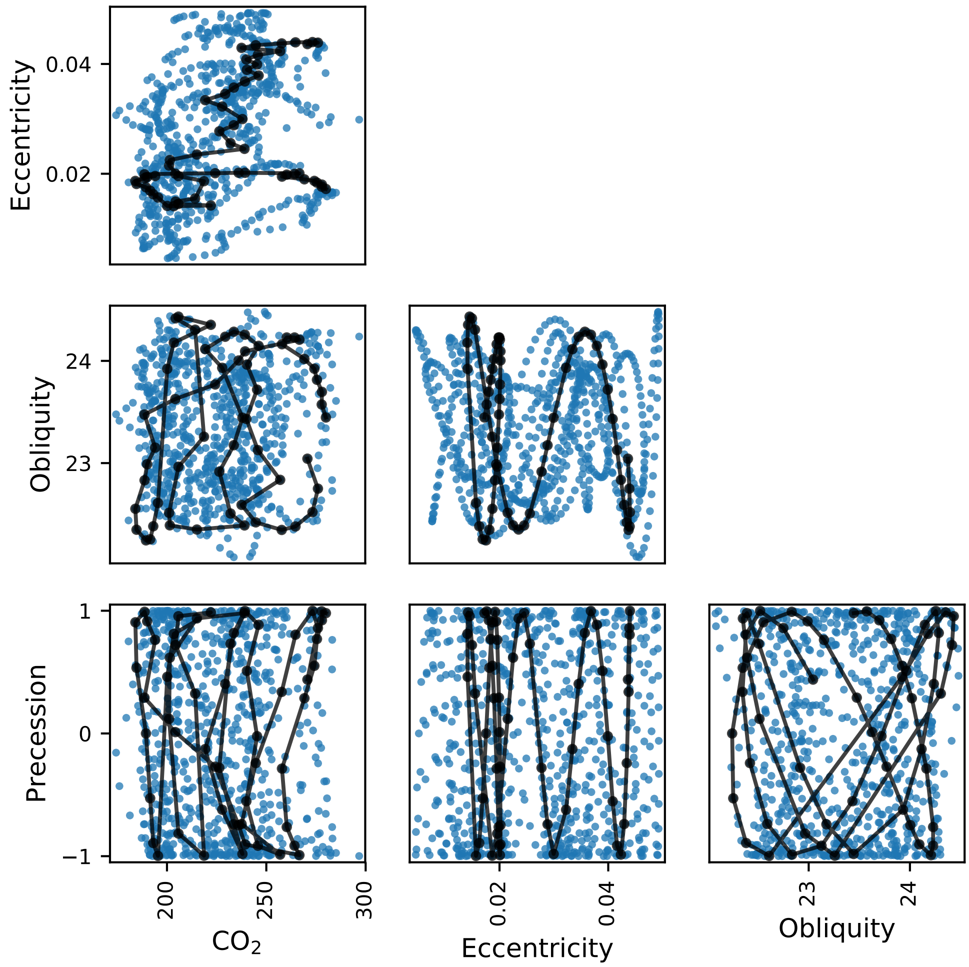

Extended Data Figure 4: Parameter space of the four independent variables (i.e., external forcing or regressors) as scatter plot matrix for last 800 ka (blue dots). The black dots highlight the location of the independent variables er sets of the 58 HadCM3 snapshot simulations which we used as training data (80% of the total 72) for the linear regression model.

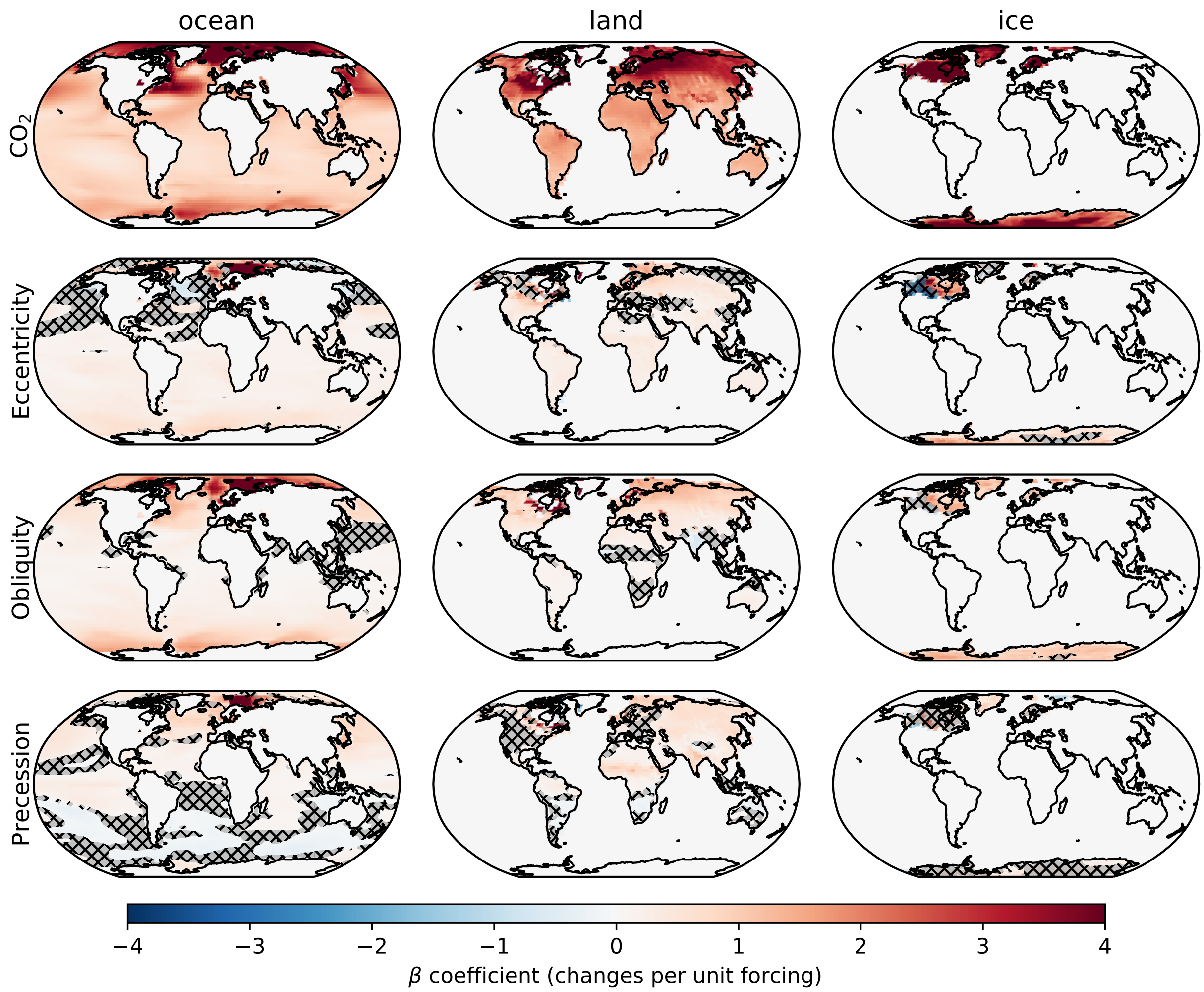

Extended Data Figure 5: Regression coefficients for mean annual temperature. Regions where the respective coefficient is not statistically significant ($p < 0.05$) are hatched and shaded.

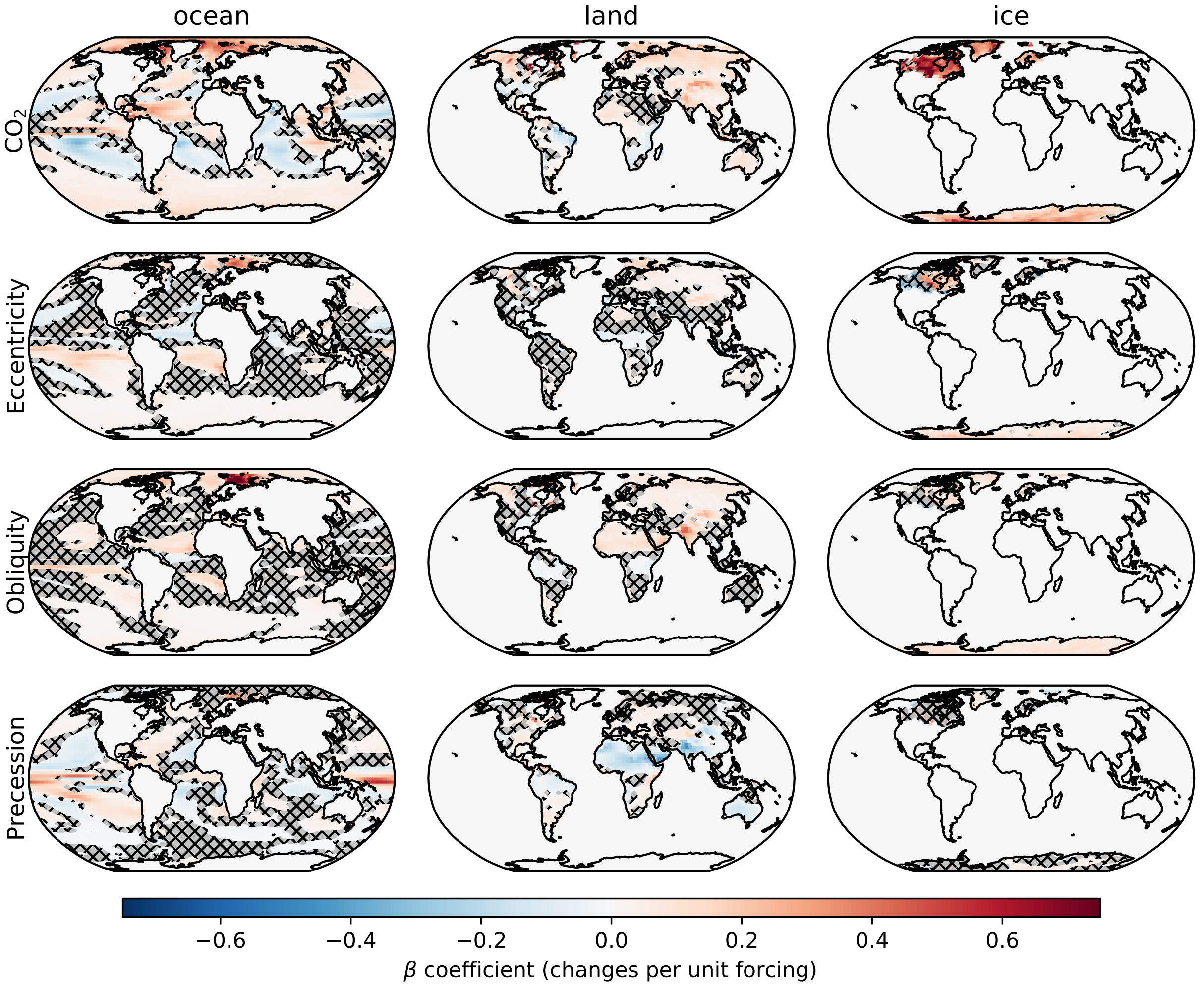

Extended Data Figure 6: Regression coefficients for mean annual precipitation. Regions where the respective coefficient is not statistically significant ($p < 0.05$) are hatched and shaded.

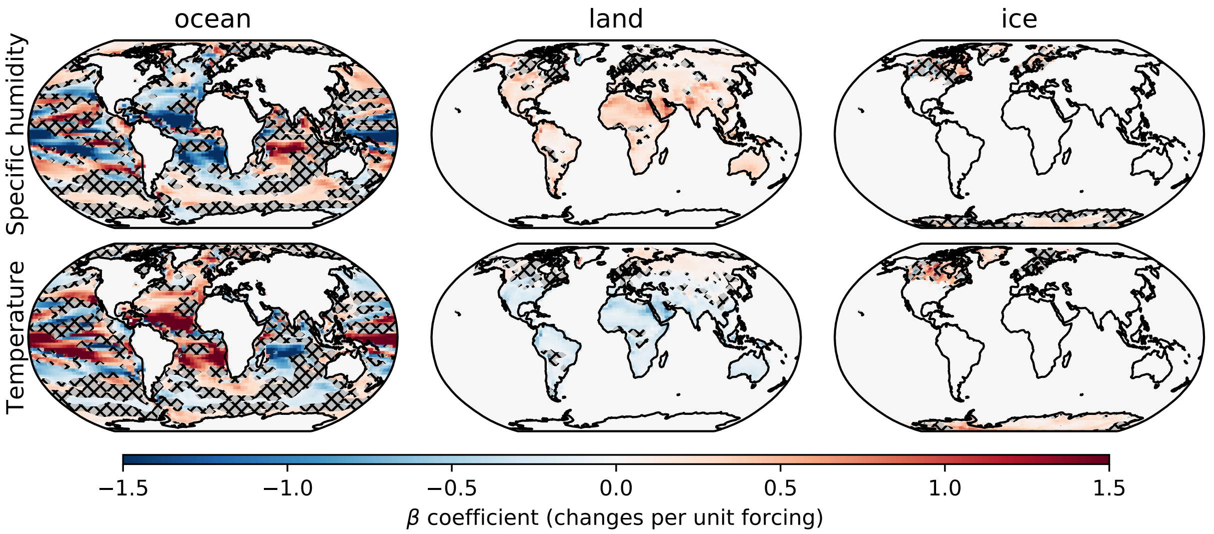

Extended Data Figure 7: Regression coefficients for mean annual precipitation with alternative independent variables temperature and specific humidity. Regions where the respective coefficient is not statistically significant ($p < 0.05$) are hatched and shaded.

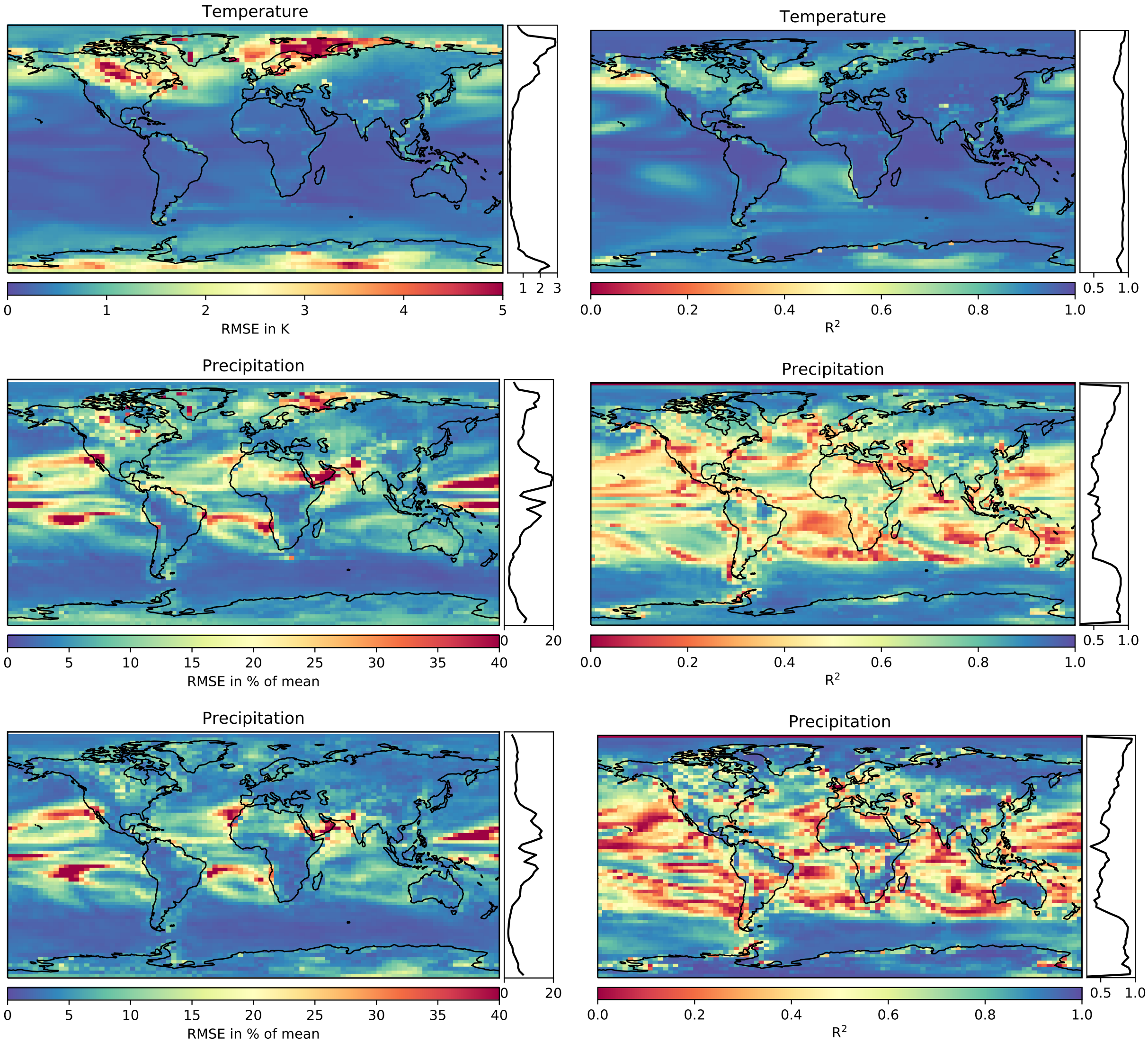

Extended Data Figure 8: R^2 values as estimator for the goodness of the model (higher is better) using the training data, and root mean square errors (RMSE) as estimators of the goodness of fit (lower is better) using the test data. Shown are the R^2 and RMSEs for mean annual temperature, precipitation, and the alternative model for precipitation—based on temperature and specific humidity.

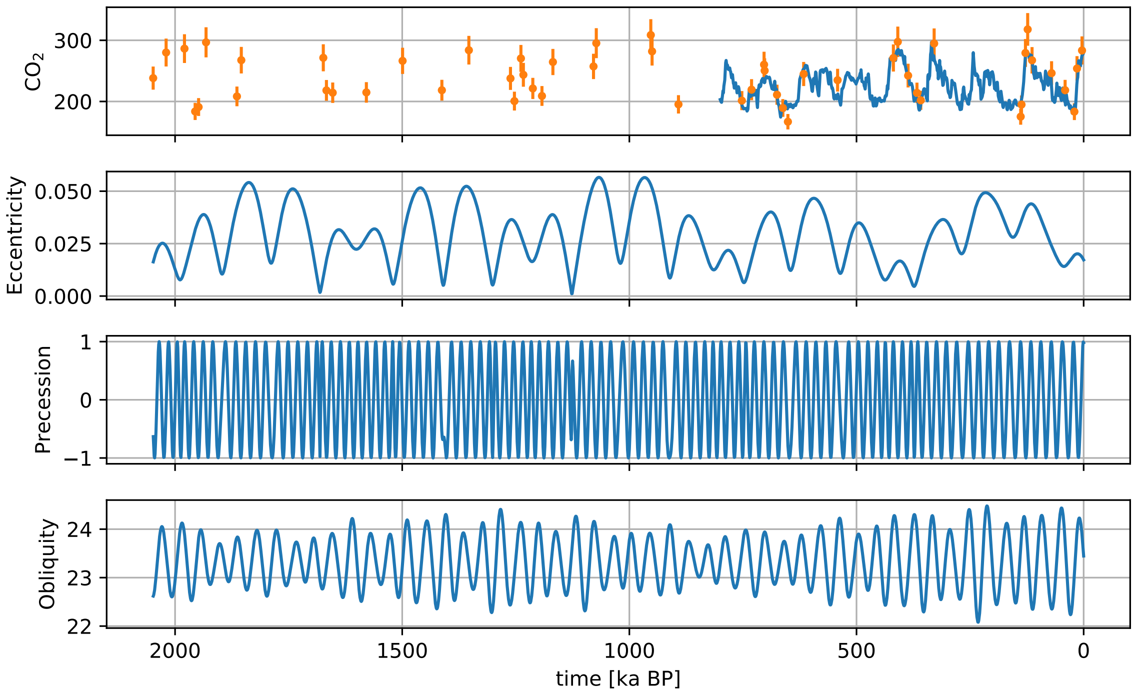

Extended Data Figure 9: Time series of external parameters: CO_2 and orbital parameters for the last 2 million years. The continuous CO_2 record is from the EPICA Dome C ice core in Antarctica [62]. The point-wise CO_2 record is based on boron isotopes from planktonic foraminifera [63]. The orbital parameters are numerical solutions for the Earth's orbit and rotation in terms of eccentricity, precession, and obliquity [64].

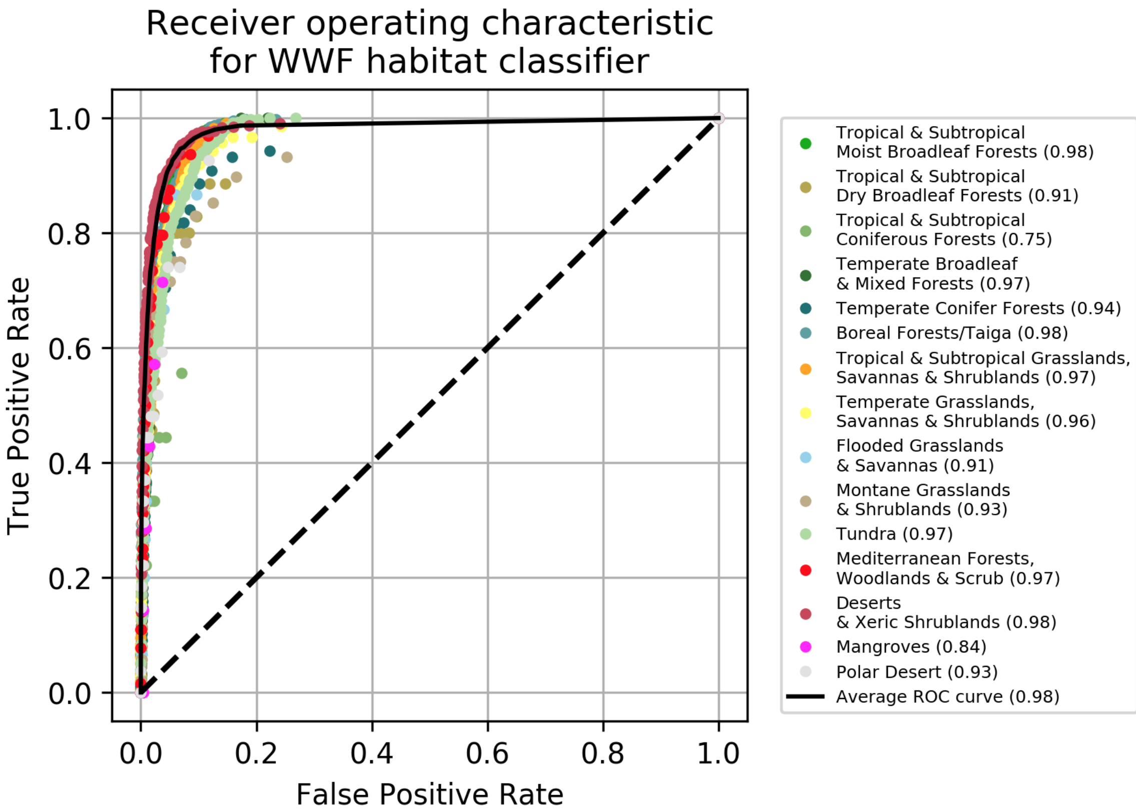

Extended Data Figure 10: A receiver operating characteristic curve for the random forest classifier of the WWF 14 major habitats. The upper left corner represents a perfect prediction of an ecosystem, while the diagonal line represents a prediction made by random guessing. The closer the ROC curve is to the perfection point (0,1) the better the random forest classification is.

References

[25] Past Interglacials Working Group of PAGES. Interglacials of the last 800,000 years. *Reviews of Geophysics*, 54(1):2015RG000482, March 2016.

[26] Keiji Horikawa, Masafumi Murayama, Masao Minagawa, Yoshihisa Kato, and Takuya Sagawa. Latitudinal and downcore (0–750 ka) changes in n-alkane chain lengths in the eastern equatorial Pacific. *Quaternary Research*, 73(3):573–582, May 2010.

[27] Bruce W. Hayward, Ashwaq T. Sabaa, Andrew Kolodziej, Martin P. Crundwell, Silke Steph, George H. Scott, Helen L. Neil, Helen C. Bostock, Lionel Carter, and Hugh R. Grenfell. Planktic foraminifera-based sea-surface temperature record in the Tasman Sea and history of the Subtropical Front around New Zealand, over the last one million years. *Marine Micropaleontology*, 82-83:13–27, January 2012.

[28] Bruce W. Hayward, George H. Scott, Martin P. Crundwell, James P. Kennett, Lionel Carter, Helen L. Neil, Ashwaq T. Sabaa, Kate Wilson, J. Stuart Rodger, Grace Schaefer, Hugh R. Grenfell, and Qianyu Li. The effect of submerged plateaux on Pleistocene gyral circulation and sea-surface temperatures in the Southwest Pacific. *Global and Planetary Change*, 63(4):309–316, October 2008.

[29] Martin Crundwell, George Scott, Tim Naish, and Lionel Carter. Glacial–interglacial ocean climate variability from planktonic foraminifera during the Mid-Pleistocene transition in the temperate Southwest Pacific, ODP Site 1123. *Palaeogeography, Palaeoclimatology, Palaeoecology*, 260(1):202–229, April 2008.

[30] Zhonghui Liu. *Pleistocene climate evolution in the eastern Pacific and implications for the orbital theory of climate change*. Ph.D., Brown University, United States – Rhode Island, 2004.

[31] K. A. Dyez, A. C. Ravelo, and A. C. Mix. Evaluating drivers of Pleistocene eastern tropical Pacific sea surface temperature. *Paleoceanography*, 31(8):1054–1069, July 2016.

[32] Kira T. Lawrence, Timothy D. Herbert, Catherine M. Brown, Maureen E. Raymo, and Alan M. Haywood. High-amplitude variations in North Atlantic sea surface temperature during the early Pliocene warm period. *Paleoceanography*, 24(2):PA2218, June 2009.

[33] T. D. Herbert. Collapse of the California Current During Glacial Maxima Linked to Climate Change on Land. *Science*, 293(5527):71–76, July 2001.

[34] Timothy D. Herbert, Laura Cleaveland Peterson, Kira T. Lawrence, and Zhonghui Liu. Tropical Ocean Temperatures Over the Past 3.5 Million Years. *Science*, 328(5985):1530–1534, June 2010.

[35] Li Li, Qianyu Li, Jun Tian, Pinxian Wang, Hui Wang, and Zhonghui Liu. A 4-Ma record of thermal evolution in the tropical western Pacific and its implications on climate change. *Earth and Planetary Science Letters*, 309(1):10–20, September 2011.

[36] Alfredo Martínez-Garcia, Antoni Rosell-Melé, Walter Geibert, Rainer Gersonde, Pere Masqué, Vania Gaspari, and Carlo Barbante. Links between iron supply, marine productivity, sea surface temperature, and CO2 over the last 1.1 Ma. *Paleoceanography*, 24(1), February 2009.

[37] Zhonghui Liu, Mark A. Altabet, and Timothy D. Herbert. Glacial-interglacial modulation of eastern tropical North Pacific denitrification over the last 1.8-Myr. *Geophysical Research Letters*, 32(23), December 2005.

[38] Johan Etourneau, Philippe Martinez, Thomas Blanz, and Ralph Schneider. Pliocene–Pleistocene variability of upwelling activity, productivity, and nutrient cycling in the Benguela region. *Geology*, 37(10):871–874, October 2009.

[39] T. Russon, M. Elliot, A. Sadekov, G. Cabioch, T. Corrège, and P. De Deckker. Inter-hemispheric asymmetry in the early Pleistocene Pacific warm pool. *Geophysical Research Letters*, 37(11), June 2010.

[40] Alfredo Martínez-Garcia, Antoni Rosell-Melé, Erin L. McClymont, Rainer Gersonde, and Gerald H. Haug. Subpolar Link to the Emergence of the Modern Equatorial Pacific Cold Tongue. *Science*, 328(5985):1550–1553, June 2010.

[41] T. Caley, J.-H. Kim, B. Malaizé, J. Giraudeau, T. Laepple, N. Caillon, K. Charlier, H. Rebaubier, L. Rossignol, I. S. Castañeda, S. Schouten, and J. S. Sinninghe Damsté. High-latitude obliquity as a dominant forcing in the Agulhas current system. *Clim. Past*, 7(4):1285–1296, November 2011.

[42] Dirk Nürnberg and Jeroen Groeneveld. Pleistocene variability of the Subtropical Convergence at East Tasman Plateau: Evidence from planktonic foraminiferal Mg/Ca (ODP Site 1172a). *Geochemistry, Geophysics, Geosystems*, 7(4), April 2006.

[43] Grace Schaefer, J. Stuart Rodger, Bruce W. Hayward, James P. Kennett, Ashwaq T. Sabaa, and George H. Scott. Planktic foraminiferal and sea surface temperature record during the last 1 Myr across the Subtropical Front, Southwest Pacific. *Marine Micropaleontology*, 54(3-4):191–212, March 2005.

[44] W. F. Ruddiman, M. E. Raymo, D. G. Martinson, B. M. Clement, and J. Backman. Pleistocene evolution: Northern hemisphere ice sheets and North Atlantic Ocean. *Paleoceanography and Paleoclimatology*, 4(4):353–412, August 1989.

[45] Sze Ling Ho, Gesine Mollenhauer, Frank Lamy, Alfredo Martínez-Garcia, Mahyar Mohtadi, Rainer Gersonde, Dierk Hebbeln, Samuel Nunez-Ricardo, Antoni Rosell-Melé, and Ralf Tiedemann. Sea surface temperature variability in the Pacific sector of the Southern Ocean over the past 700 kyr. *Paleoceanography*, 27(4), October 2012.

[46] K. A. Dyez and A. C. Ravelo. Late Pleistocene tropical Pacific temperature sensitivity to radiative greenhouse gas forcing. *Geological Society of America*, 41(1):23–26, January 2013.

[47] Martín Medina-Elizalde and David W Lea. The Mid-Pleistocene Transition in the Tropical Pacific. *Science (New York, N.Y.)*, 310:1009–12, December 2005.

[48] J. Warren Beck, Weijian Zhou, Cheng Li, Zhenkun Wu, Lara White, Feng Xian, Xianghui Kong, and Zhisheng An. A 550,000-year record of East Asian monsoon rainfall from 10be in loess. *Science*, 360(6391):877–881, May 2018.

[49] Miryam Bar-Matthews, Avner Ayalon, Mabs Gilmour, Alan Matthews, and Chris J. Hawkesworth. Sea–land oxygen isotopic relationships from planktonic foraminifera and speleothems in the Eastern Mediterranean region and their implication for paleorainfall during interglacial intervals. *Geochimica et Cosmochimica Acta*, 67(17):3181–3199, September 2003.

[50] Martin Melles, Julie Brigham-Grette, Pavel S. Minyuk, Norbert R. Nowaczyk, Volker Wennrich, Robert M. DeConto, Patricia M. Anderson, Andrei A. Andreev, Anthony Coletti, Timothy L. Cook, Eeva Haltia-Hovi, Maaret Kukkonen, Anatoli V. Lozhkin, Peter Rosén, Pavel Tarasov, Hendrik Vogel, and Bernd Wagner. 2.8 Million Years of Arctic Climate Change from Lake El'gygytgyn, NE Russia. *Science*, 337(6092):315–320, July 2012.

[51] Z. T. Guo, A. Berger, Q. Z. Yin, and L. Qin. Strong asymmetry of hemispheric climates during MIS-13 inferred from correlating China loess and Antarctica ice records. *Clim. Past*, 5(1):21–31, February 2009.

[52] Nicolas Waldmann, Adi Torfstein, and Mordechai Stein. Northward intrusions of low- and mid-latitude storms across the Saharo-Arabian belt during past interglacials. *Geology*, 38(6):567–570, June 2010.

[53] Landwehr, J.m, Sharp, W.D, Coplen, T.B, Ludwig, K.R, and Winograd, I.J. The Chronology for the δ^{18}O Record from Devils Hole, Nevada, Extended Into the Mid-Holocene. Open Report 1082, U.S. Geological Survey Open-File Report, 2011.

[54] A. Vaks, M. Bar-Matthews, A. Ayalon, A. Matthews, A. Frumkin, U. Dayan, L. Halicz, A. Almogi-Labin, and B. Schilman. Paleoclimate and location of the border between Mediterranean climate region and the Saharo–Arabian Desert as revealed by speleothems from the northern Negev Desert, Israel. *Earth and Planetary Science Letters*, 249(3):384–399, September 2006.

[55] Qingzhen Hao, Luo Wang, Frank Oldfield, Shuzhen Peng, Li Qin, Yang Song, Bing Xu, Yansong Qiao, Jan Bloemendal, and Zhengtang Guo. Delayed build-up of Arctic ice sheets during 400,000-year minima in insolation variability. *Nature*, 490(7420):393–396, October 2012.

[56] Elizabeth K. Thomas, Steven C. Clemens, Youbin Sun, Warren L. Prell, Yongsong Huang, Lee Gao, Shannon Loomis, Guangshan Chen, and Zhengyu Liu. Heterodynes dominate precipitation isotopes in the East Asian monsoon region, reflecting interaction of multiple climate factors. *Earth and Planetary Science Letters*, 455, October 2016.

[57] J. Jouzel, V. Masson-Delmotte, O. Cattani, G. Dreyfus, S. Falourd, G. Hoffmann, B. Minster, J. Nouet, J. M. Barnola, J. Chappellaz, H. Fischer, J. C. Gallet, S. Johnsen, M. Leuenberger, L. Loulergue, D. Luethi, H. Oerter, F. Parrenin, G. Raisbeck, D. Raynaud, A. Schilt, J. Schwander, E. Selmo, R. Souchez, R. Spahni, B. Stauffer, J. P. Steffensen, B. Stenni, T. F. Stocker, J. L. Tison, M. Werner, and E. W. Wolff. Orbital and Millennial Antarctic Climate Variability over the Past 800,000 Years. *Science*, 317(5839):793–796, August 2007.

[58] H. Cheng, P. Z. Zhang, C. Spötl, R. L. Edwards, Y. J. Cai, D. Z. Zhang, W. C. Sang, M. Tan, and Z. S. An. The climatic cyclicity in semiarid-arid central Asia over the past 500,000 years. *Geophysical Research Letters*, 39(1), January 2012.

[59] Stacy A. Carolin, Kim M. Cobb, Jean Lynch-Stieglitz, Jessica W. Moerman, Judson W. Partin, Syria Lejau, Jenny Malang, Brian Clark, Andrew A. Tuen, and Jess F. Adkins. Northern Borneo stalagmite records reveal West Pacific hydroclimate across MIS 5 and 6. *Earth and Planetary Science Letters*, 439:182–193, April 2016.

[60] P. C. Tzedakis, H. Hooghiemstra, and H. Pälike. The last 1.35 million years at Tenaghi Philippon: revised chronostratigraphy and long-term vegetation trends. *Quaternary Science Reviews*, 25(23):3416–3430, December 2006.

[61] Hai Cheng, R. Lawrence Edwards, Ashish Sinha, Christoph Spötl, Liang Yi, Shitao Chen, Megan Kelly, Gayatri Kathayat, Xianfeng Wang, Xianglei Li, Xinggong Kong, Yongjin Wang, Youfeng Ning, and Haiwei Zhang. The Asian monsoon over the past 640,000 years and ice age terminations. *Nature*, 534(7609):640–646, June 2016.

[62] Bernhard Bereiter, Sarah Eggleston, Jochen Schmitt, Christoph Nehrbass-Ahles, Thomas F. Stocker, Hubertus Fischer, Sepp Kipfstuhl, and Jerome Chappellaz. Revision of the EPICA Dome C CO2 record from 800 to 600 kyr before present. *Geophysical Research Letters*, 42(2):2014GL061957, January 2015.

[63] Bärbel Hönisch, N. Gary Hemming, David Archer, Mark Siddall, and Jerry F. McManus. Atmospheric Carbon Dioxide Concentration Across the Mid-Pleistocene Transition. *Science*, 324(5934):1551–1554, June 2009.

[64] A. Berger and M. F. Loutre. Insolation values for the climate of the last 10 million years. *Quaternary Science Reviews*, 10(4):297–317, January 1991.